ADVANCED MATERIALS
www.advmat.de

Engineering of Living Cells with Polyphenol-Functionalized Biologically Active Nanocomplexes

Zongmin Zhao, Daniel C. Pan, Qin M. Qi, Jayoung Kim, Neha Kapate, Tao Sun, C. Wyatt Shields IV, Lily Li-Wen Wang, Debra Wu, Christopher J. Kwon, Wei He, Junling Guo, and Samir Mitragotri**

Approaches to safely and effectively augment cellular functions without compromising the inherent biological properties of the cells, especially through the integration of biologically labile domains, remain of great interest. Here, a versatile strategy to assemble biologically active nanocomplexes, including proteins, DNA, mRNA, and even viral carriers, on cellular surfaces to generate a cell-based hybrid system referred to as "Cellnex" is established. This strategy can be used to engineer a wide range of cell types used in adoptive cell transfers, including erythrocytes, macrophages, NK cells, T cells, etc. Erythrocyte$_{nex}$ can enhance the delivery of cargo proteins to the lungs in vivo by 11-fold as compared to the free cargo counterpart. Biomimetic microfluidic experiments and modeling provided detailed insights into the targeting mechanism. In addition, Macrophage$_{nex}$ is capable of enhancing the therapeutic efficiency of anti-PD-L1 checkpoint inhibitors in vivo. This simple and adaptable approach may offer a platform for the rapid generation of complex cellular systems.

Cell-based therapies, comprising administration of living cells to patients for direct therapeutic activities, have experienced remarkable success in the clinic.[1–4] Chimeric antigen receptor (CAR) T cell therapies in particular have led to improved remission rates in patients with multiple myeloma, leukemia, lymphomas, melanoma, cervical cancer, bile duct cancer, and neuroblastoma compared to traditional chemotherapeutic regimens.[5–8] New treatment strategies implementing erythrocytes, macrophages, monocytes, natural killer (NK) cells, and pluripotent stem cells are in various stages of development for the treatment of cancer, chronic infections, and autoimmune disorders.[9] However, many of these strategies rely on the genetic alteration and expansion of cells, which requires several weeks of preparation.[10] For example, CAR T cell therapies require a preparation time of at least three weeks, which can be prohibitively long for patients with advanced or metastatic cancers.[11,12] Thus, there is a broad interest in engineering functional cells ex vivo in a manner that is rapid, scalable, and agnostic to the therapeutic cell of interest.[10,13]

One approach to addressing this challenge is the concurrent delivery of biomolecules through the integration of carried nanoparticles (e.g., "hitchhiking" or "backpack" systems) on the surface of living cells to improve therapeutic potency.[14–19] This strategy has shown promising results in preclinical studies,[20–23] however, the stable attachment of nanoparticles to cell surfaces often relies on interactions that only work for certain cell types in specific particle–cell combinations (e.g., electrostatic, hydrophobic, hyaluronan–CD44, and antibody–antigen interactions).[10,24] Moreover, though some methods allow the formation of functional thin films around the cells, such as layer-by-layer (LbL) assemblies or surface-initiated polymerization around cells,[25–27] these techniques

Dr. Z. Zhao, Dr. D. C. Pan, Dr. Q. M. Qi, Dr. J. Kim, N. Kapate, Dr. T. Sun, Prof. C. W. Shields IV,[+] L. L.-W. Wang, Dr. D. Wu, C. J. Kwon, Prof. W. He, Prof. J. Guo,[++] Prof. S. Mitragotri
John A. Paulson School of Engineering and Applied Sciences
Harvard University
Cambridge, MA 02138, USA
E-mail: junling.guo@scu.edu.cn; mitragotri@seas.harvard.edu

The ORCID identification number(s) for the author(s) of this article can be found under https://doi.org/10.1002/adma.202003492.

[+]Present address: Department of Chemical and Biological Engineering, University of Colorado Boulder, Boulder, CO 80309, USA

[++]Present address: BMI Center for Biomass Materials and Nanointerfaces, School of Biomass Science and Engineering, Sichuan University, Chengdu 610035, China

Dr. Z. Zhao, Dr. D. C. Pan, Dr. Q. M. Qi, Dr. J. Kim, Prof. C. W. Shields IV,[+] Prof. J. Guo,[++] Prof. S. Mitragotri
Wyss Institute for Biologically Inspired Engineering
Harvard University
Boston, MA 02115, USA

N. Kapate, L. L.-W. Wang
Harvard-MIT Division of Health Sciences and Technology
Massachusetts Institute of Technology
Cambridge, MA 02139, USA

Dr. T. Sun
Department of Radiology
Brigham and Women's Hospital
Harvard Medical School
Boston, MA 02115, USA

DOI: 10.1002/adma.202003492

could either completely alter the surface biological identities of cells (e.g., blocking cell receptors), or act as case-by-case strategies to overcome the difference of payload molecules and cell types. Currently, no platform exists to functionalize a wide range of mammalian cells with a wide range of biomolecules in a simple, scalable manner.[28] Therefore, there is an urgent need to develop a strategy to integrating biologically active molecules on cell surfaces that can be applied to a broad range of cell types and biomolecular payloads, while reducing timescales necessary for preparing the biohybrid cellular systems.

In previous work, Guo et al. have developed a modular approach to assemble colloidal building blocks into superstructures via polyphenol-based surface functionalization of a wide range of nanoparticles followed by an interfacial assembly on secondary template particles.[29] This method further allowed the development of a bioinorganic hybrid platform that consists of highly efficient light-harvesting semiconductor nanoparticles and genetically engineered yeast cells.[30] These previous studies inspired us about the possibility of extending the building blocks to biological molecules and assembling them on the surface of mammalian cells to create a versatile cell-based biological platform in which extrinsic bioactive functionalities can be imparted to cells. Here, we report the use of a polyphenol-based molecular engineering strategy as a rapid and efficient approach to functionalize cell surfaces with a range of payloads to integrate the biological functions of biomolecules and cellular systems that we refer to as "Cellnex." The polyphenol moieties integrated with the biomolecules (**Figure 1**a) can facilitate the assembly of biologically active nanocomplexes on cell surfaces directed by a metal–phenolic coordination-mediated interfacial interaction (Figure 1b,c).[29,31] This simple and modular approach enabled the functionalization of erythrocytes with at least 10 biomolecules, including functional proteins, DNA, mRNA, and viral carriers without compromising the inherent biological properties of the cells. Several other cell types including T cells, monocytes, macrophages, dendritic cells, and NK cells were also engineered to their corresponding Cellnex variants, demonstrating a customizable cell-engineering platform with flexible toolboxes of carried biomolecules and cells for a wide range of cell-based therapies and biohybrid cell engineering.

We first investigated the feasibility of forming biomolecule nanocomplexes through polyphenol–biomolecule interactions by using a protein (bovine serum albumin, BSA) as the model biomolecule. We found that the protein nanocomplex stability depended on the stoichiometric ratios of tannic acid and functionalized proteins (Figure S1, Supporting Information). A critical stoichiometric ratio of 570 was established, below which the size of nanocomplexes was less than 10 nm. The hydrodynamic size of the nanocomplexes dramatically increased for ratios above the critical stoichiometric ratio and eventually increased to ≈900 nm for a ratio of 1900. Therefore, a minimal concentration of tannic acid was chosen to form the nanoscale complexes.[32] Figure S2 (Supporting Information) shows no aggregation for a stoichiometric ratio of 190 when the tannic acid concentration is 0.2 mg mL^{-1}, so this ratio was used in the following experiments. The ultra-small nanocomplexes (7.2 ± 0.4 nm, Figure S3, Supporting Information) are of a favorable size range for the formation of uniform nanoscale networks on the cell surfaces without blocking cellular receptors and molecular exchangeability as shown later in the biocompatibility and cellular sensing performance tests.

We selected erythrocytes as the initial example of Cellnex design, considering that erythrocyte-based therapies are an emerging platform for vascular drug delivery due to their biocompatibility and clinical safety of transfusion[33–38] (Figure 1d–f). The simple mixing of polyphenol-functionalized nanocomplexes with erythrocytes (Figure 1d) resulted in the assembly of these nanocomplexes on their surfaces to form an erythrocyte-based biohybrid system named as $Erythrocyte_{nex}$ (Figure 1e). Based on previous studies,[29] the addition of Fe^{3+} ions can induce the metal–phenolic coordination-mediated assembly of the nanocomplexes on the cellular surfaces due to the decrease of electrostatic repulsion of nanocomplexes. The zeta potential (ξ) of polyphenol-functionalized OVA nanocomplexes was −10.53 ± 0.37 mV which enables the colloidal stability of nanocomplexes. While, after the addition of Fe^{3+} ions, the zeta potential of the nanocomplexes dramatically shifted to a much less charged value of −6.4 ± 0.19 mV. Simultaneously, it is likely that the multiple interactions between the polyphenol moieties of nanocomplexes and cell surfaces facilitate the attraction driving force of rapid interfacial assembly,[29,39] such as the possible electrostatic interaction between hydroxyl groups of polyphenols and polar head structure of cell membrane lipids, and hydrophobic interaction between aromatic structure of phenolic groups and fatty acid chain of lipids.[40] The entire preparation process can be achieved within 5–10 min, demonstrating an exceptionally simple and platform process for the use of Cellnex therapies in the potential clinical applications. For instance, the biologically functional nanocomplexes can be prepared and stored in a ready-to-use status, followed by the rapid engineering of biohybrid functional cells when the donor cells are ready.

Figure 1f shows the greater versatility of the toolbox of biomolecules used for the cellular integration, due to the multiple molecular interactions between polyphenols and biomolecules (e.g., protein, DNA, alkaloid, polysaccharide, anthocyanin, lipid).[39,40] The simplicity and modularity of Cellnex enabled the assembly of 10 representative biomolecules and viral carriers (Figure S4, Supporting Information), with different molecular sizes, charges, levels of hydrophobicity, and functionalities. In the absence of polyphenol-functionalized nanocomplexes, the negligible fluorescence signal on the surfaces of cells revealed that the nonspecific adsorption of biomolecules on cell surfaces could not achieve the formation of uniform and high loading of carried biomolecules (Figure S5, Supporting Information). We categorize these cargos to four groups: proteins (including ovalbumin, serum albumin, antibody, cholera toxin subunit B), nucleic acids (including coded DNA, mRNA),[41] bioconjugators (including streptavidin, biotin, and lectin), and viral carriers. The robustness of the Cellnex technique suggests that the polyphenol-based assembly strategy generates a versatile interfacial attractive force with the surfaces of many cell types, which is a major challenge in current particle-based "hitchhiking" or "backpack" systems.[19]

Next, we studied the impact of the assembly strategy on the stability and activity of the carried biomolecules. **Figure 2**a showed the maintenance of α-helix structure of a model protein (bovine serum albumin, BSA) after the polyphenol

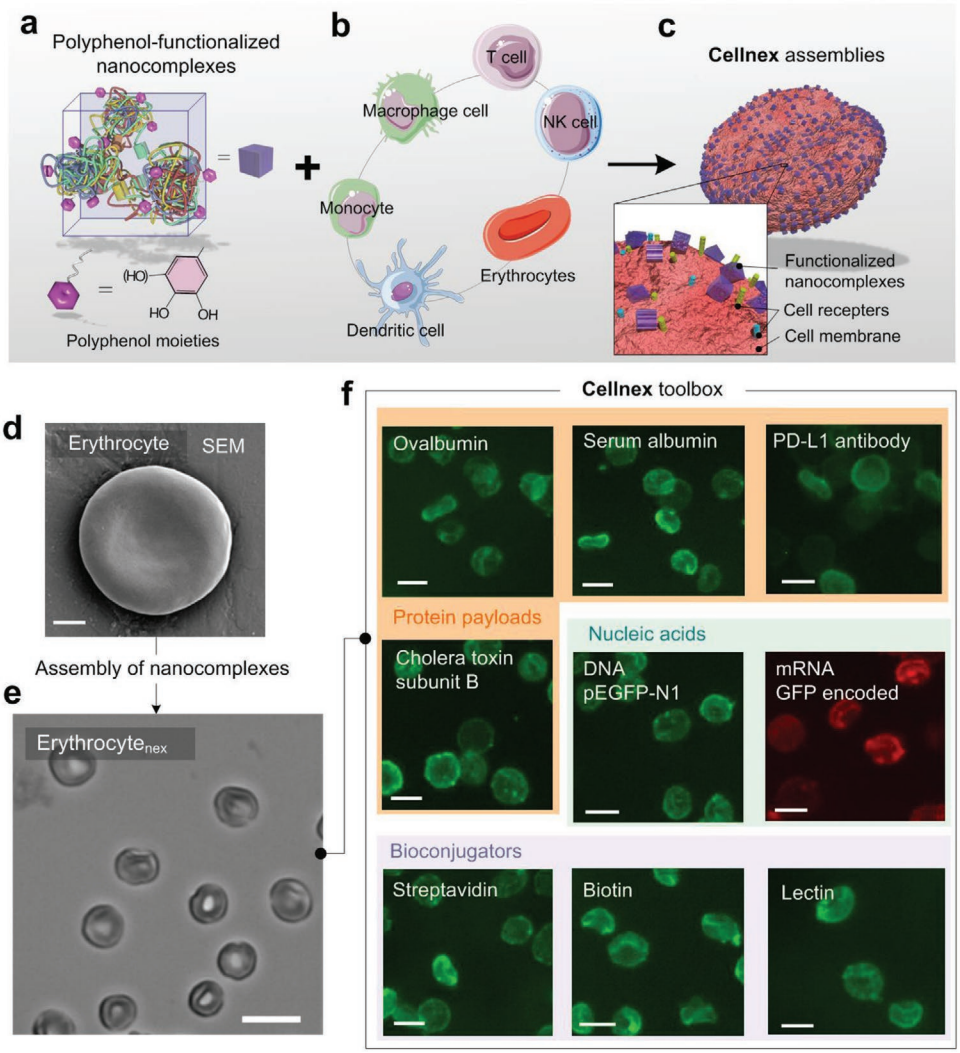

Figure 1. Modular assembly of "Cellnex" through the assembly of polyphenol-functionalized biologically active nanocomplexes on cells. a) Schematic diagram of the complexation between biomolecules and polyphenols. The polyphenol moieties can functionalize the biomolecules and enable an interfacial assembly of nanocomplexes on cell surfaces to form nanostructured networks. b) Versatile toolbox of cellular systems. We demonstrate the surface engineering of seven types of cells, including majorly circulatory and immune cells. c) The assembled biomolecule-cell complex (Cellnex) through the polyphenol-directed interfacial interactions on the surface of a cell. d) Scanning electron microscopy (SEM) image of a naïve erythrocyte. e) Optical microscopy image of Erythrocyte$_{nex}$ integrated with ovalbumin (OVA). Erythrocyte$_{nex}$ maintained the characteristic geometry of naïve erythrocytes with a typical concaved structure. f) A wide range of biomolecules were used to demonstrate the versatile toolbox of biological payloads for the Cellnex. The biomolecules were conjugated with fluorescent tags (Alexa Fluor 488, FITC, or MFP 488) for the fluorescence microscopy imaging. This toolbox includes three main categories of biomolecules, including proteins, nucleic acids, and biological conjugators. Scale bars are 1 µm (d) and 5 µm ((e) and (f)).

functionalization.[32] Enzyme-linked immunosorbent assay (ELISA) further demonstrated the preservation of biological activity of interleukin-4 (IL-4, a representative protein that is highly sensitive to denaturation) after polyphenol-based functionalization (Figure 2b). Transmission electron microscopy (TEM) images show the nanostructural change of the erythrocyte surfaces. The reconstructed intensity map and line images reveal the formation of interconnecting network of nanocomplexes on the cell surface (Figure 2c and Figure S6, Supporting Information). In addition, attachment of protein nanocomplexes to Erythrocyte$_{nex}$ was also confirmed by flow cytometry. 96.7% ± 2.4% of the erythrocytes carried cargo proteins (Figure S7, Supporting Information). The amount of the biological active species can be tuned by simply changing the added concentrations of corresponding nanocomplexes (Figure S8, Supporting Information). The disassembly of metal-phenolic network of the nanocomplexes on cell surfaces enables a two-phase release kinetics of the attached protein.[42] An initial relatively fast release of carried protein was observed during the first 4 h, as nearly 65% and 90% of protein was released in two physiological conditions including PBS (with 5×10^{-3} M glucose) and fetal bovine serum (FBS). At longer time periods, the remaining protein profiled a long-term release and reached a plateau after 24 h (Figure 2d). We note that the kinetics of release can be tuned by the rational selection of different metal ions (Fe^{3+}, Al^{3+}, or Cu^{2+}), as investigated in previous work.[42]

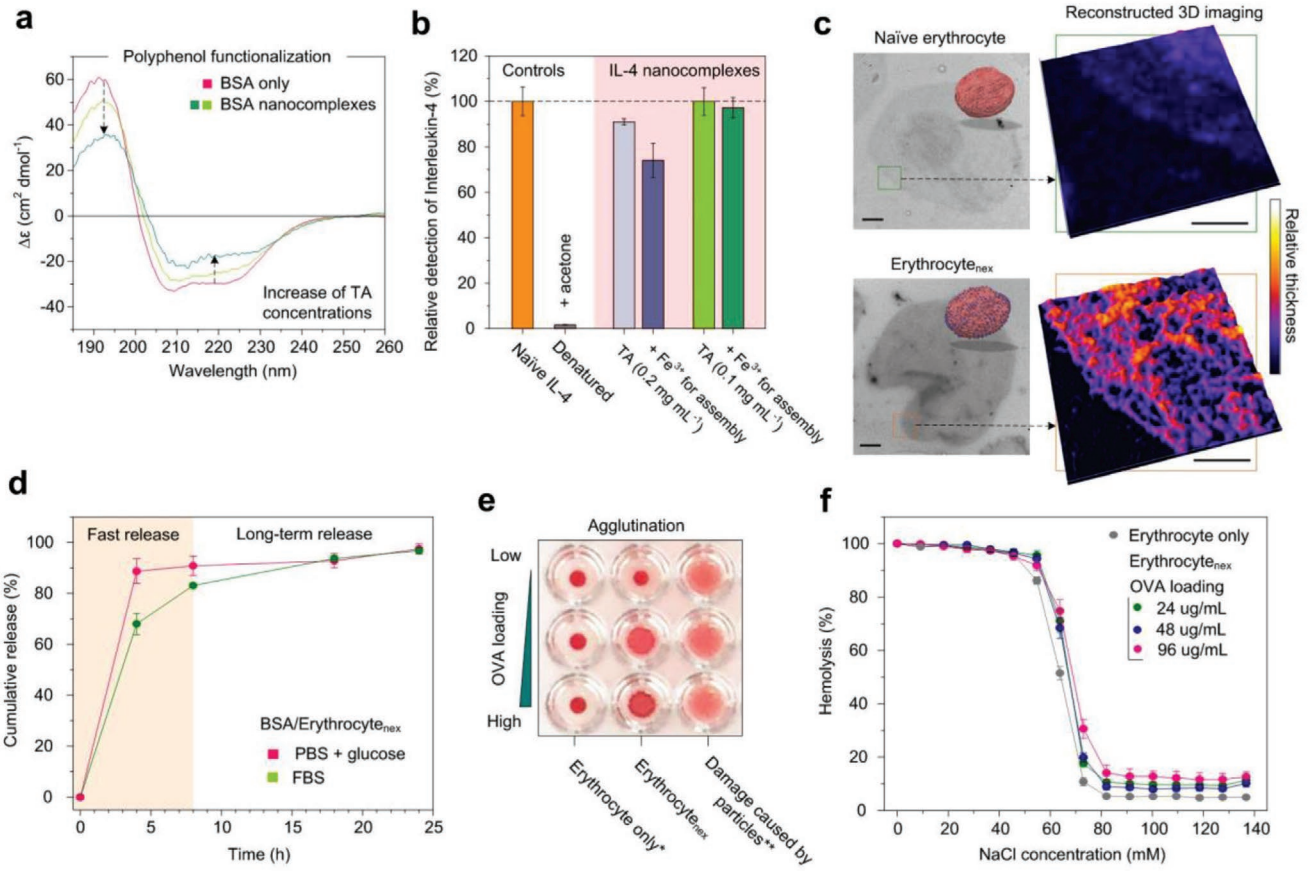

Figure 2. Engineering of Erythrocyte$_{nex}$ through the assembly of polyphenol-functionalized protein nanocomplexes on erythrocytes. a) Circular dichroism spectroscopy of BSA and polyphenol-functionalized BSA nanocomplexes. Though an increase in tannic acid concentration leads to a decrease in peak intensity, the feature of an α-helix structure maintained. b) Relative activity of interleukin-4 and the formed interleukin-4 nanocomplexes with different concentrations of tannic acid (measured by ELISA assay). The addition of Fe^{3+} (0.36 mg mL^{-1}) facilitated the interfacial assembly on the surfaces of cells during the Cellnex formation process. c) TEM images of a naïve erythrocyte and a BSA/Erythrocyte$_{nex}$. The reconstructed 3D topographic images show the formation of nanostructured networks from the polyphenol-functionalized nanocomplexes on the cell surface of Erythrocyte$_{nex}$ compared to a naïve erythrocyte. d) Cargo protein release kinetics from Erythrocyte$_{nex}$. PBS and FBS media simulate the in vitro assembly condition and serum environment, respectively. e) Agglutination of erythrocyte and OVA/Erythrocyte$_{nex}$ was visualized using a U-shaped bottom plate, with aggregated Erythrocyte$_{nex}$ forming a diffused lattice. Polystyrene nanoparticles were used as a demonstration of nanoparticle-caused cytotoxicity to erythrocytes. Low amount of OVA loading is 24 ug L^{-1}. f) Osmotic fragility curves of Erythrocyte$_{nex}$ with different amounts of polyphenol-functionalized OVA nanocomplexes after immediate exposure to different concentrations of NaCl. Inset shows the percent hemolysis at 73×10^{-3} M NaCl. Scale bars are 1 μm (c) and 200 nm ((c), magnified areas). Variation is represented by SE (error bars) from three independent replicates for all data points.

To investigate the biocompatibility of polyphenol-functionalized protein nanocomplexes on erythrocytes, we assembled different amounts of functionalized protein nanocomplexes onto erythrocytes and analyzed the overall function of the erythrocytes, including agglutination, osmotic sensitivity, mechanical fragility, and hemolysis. No aggregates were observed in naïve erythrocytes as well as erythrocytes with low amounts of protein (24 μg L^{-1}) nanocomplexes. However, the amount of aggregates appears to increase with increasing concentrations of protein nanocomplexes, but these aggregations are still less prominent as compared with those induced by carboxylated polystyrene nanoparticles (Figure 2e). Potential detrimental effects of protein nanocomplexes assembled onto erythrocyte were also investigated by the sensitivity of erythrocytes toward osmotic stress. Assembled protein nanocomplexes led to the formation of slightly sensitized erythrocytes at 1% hematocrit concentration when immediately exposed to various hypotonic solutions, indicating a slight decrease in erythrocyte sensitivity compared to naïve erythrocytes (Figure 2f). Mechanical fragility of Erythrocyte$_{nex}$ under prolonged levels of low shear stress was examined. Figure S9 (Supporting Information) shows that at 1% hematocrit, erythrocytes displayed low levels of hemolysis (≈5% at 24 h) when rotated at 37 °C. Within this period of 1 h, the assemblies of low and medium amounts of protein nanocomplexes slightly aggravated hemolysis (≈15%) compared to erythrocytes (≈5%). Furthermore, high amounts of protein nanocomplexes further induced hemolysis (25%) during this period. Therefore, we chose the optimized concentration of nanocomplexes as 24 μg L^{-1} for the preparation of Erythrocyte$_{nex}$ due to the relatively low rate of hemolysis.

Next, we examined the biodistribution of a model biomolecule (Ovalbumin, OVA) which was integrated on Erythrocyte$_{nex}$ after intravenous administrations (**Figure 3**). Biodistribution analysis revealed strong signal intensities in the liver 5 min

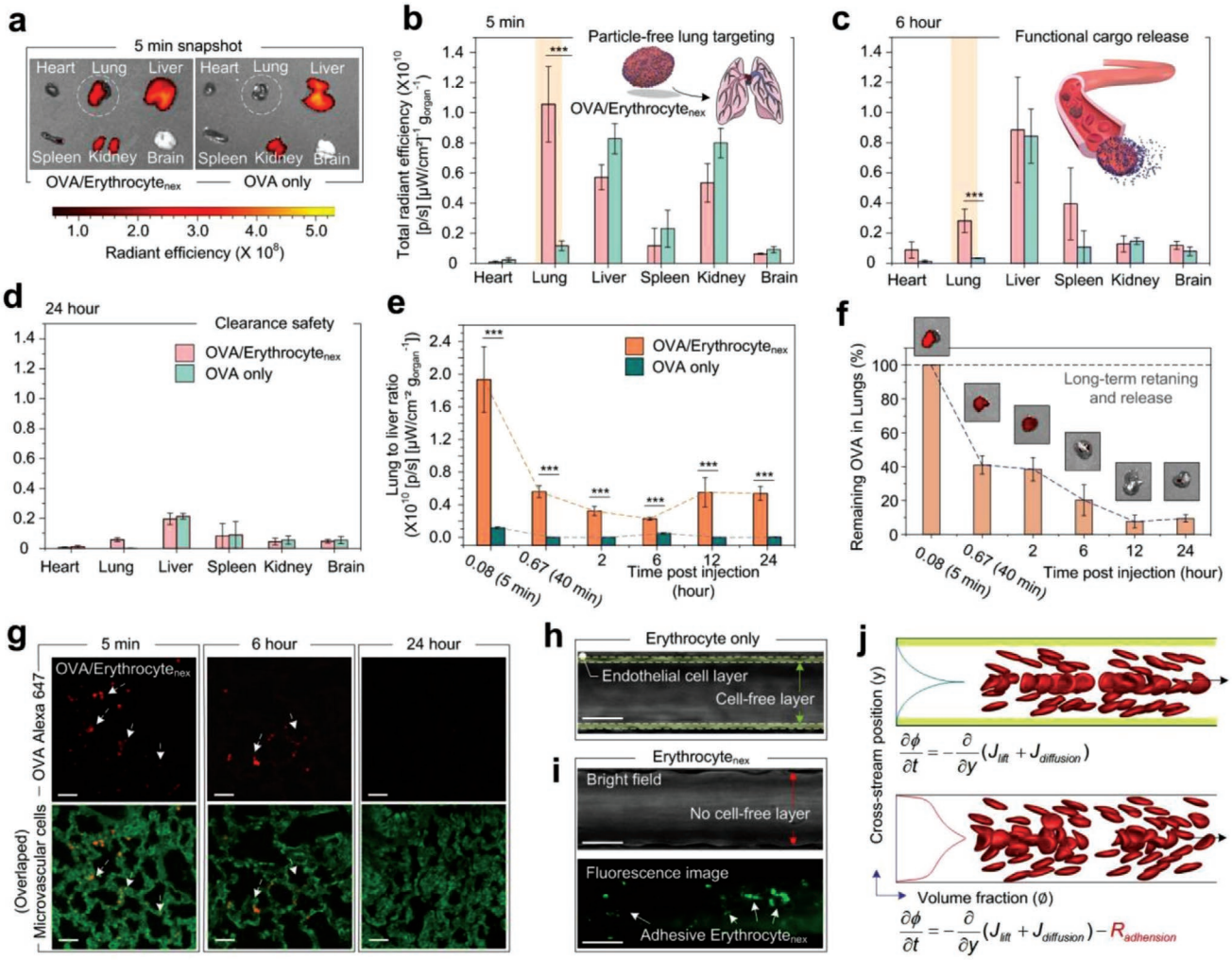

Figure 3. Erythrocyte$_{nex}$ selectively target lungs via particle-free mechanisms. a) IVIS images of excised mouse lungs 5 min (0.08 h) after the administration of OVA protein only and OVA/Erythrocyte$_{nex}$. Alexa Fluor 674-conjugated OVA was used for the fluorescence signal. b) Biodistribution of OVA only and OVA/Erythrocyte$_{nex}$ 5 min after intravenous (IV) administration. c) Biodistribution of OVA only and OVA/Erythrocyte$_{nex}$ 6 h after IV administration. d) Biodistribution of OVA only and OVA/Erythrocyte$_{nex}$ 24 h after IV administration. e) Lung to liver ratio of OVA delivered by the control counterpart and OVA/Erythrocyte$_{nex}$ throughout the entire measurement window. f) Remaining OVA delivered by Erythrocyte$_{nex}$ through the time after 24 h post-injection. Significantly different (one-way ANOVA followed by Tukey's HSD test): $^{***}p < 0.001$. Variation is represented by SE (error bars) from three independent replicates for all data points. g) Confocal fluorescence microscopy images of lung vascular capillary sections 5 min, 6 h, and 24 h after IV administration of OVA/Erythrocyte$_{nex}$. The white arrows indicate the distribution of delivered OVA. Vascular capillaries were stained by Alexa 488-conjugated anti-CD31 antibody. h) Biomimetic perfusion chamber experiments to characterize the formation of cell-free layers during the flow of naïve erythrocytes. i) Endothelial adhesive property of OVA/Erythrocyte$_{nex}$ (bottom). j) Simulations of the cross-flow distributions of naïve erythrocytes (green plot) and Erythrocyte$_{nex}$ (red plot) flowing in the vascular channels at matching mechanical properties but varying adhesive parameters. Scale bars are 50 μm in (g) and (h).

(0.08 h) after the administration of free OVA protein alone. In addition, polyphenol-functionalized OVA nanocomplexes without integration with erythrocytes were found to primarily accumulate in the liver and kidney and did not show significant accumulation in the lung at both 5 min and 2 h (Figure S10, Supporting Information). However, a significant signal increase was observed in the lungs of mice injected with OVA/Erythrocyte$_{nex}$, 11-fold higher than OVA alone. Minimal signals were detected in the heart and brain (Figure 3a,b). As time progressed, relatively high signal of OVA/Erythrocyte$_{nex}$ was still observed in the lungs 6-h post-injection (Figure 3c). 24 h post-injection, the signal of OVA carried by Erythrocyte$_{nex}$ decreased and approached the background (Figure 3d). Interestingly, Erythrocyte$_{nex}$ does not require any affinity moieties (e.g., endothelial-binding antibody) to achieve high lung uptake; the fold-increase of lung uptake ranged from ≈11-fold (from 0.08 to 6 h) to ≈140-fold (at 24 h) compared to the free OVA counterpart controls. After 0.08 h, OVA/Erythrocyte$_{nex}$ generated a high lung-to-liver ratio of ≈2, which is nearly 18-fold higher than that observed with free OVA. Moreover, after 24 h, the lung-to-liver ratio was 335-fold higher compared to the free OVA counterparts (Figure 3e). These results suggest that Erythrocyte$_{nex}$ enabled highly selective delivery of protein cargo in the lungs, sustained long release times, and eventually permitted

excretion (Figure 3f). There was little to no signal observed in the whole blood at any time points (Figure S11, Supporting Information), suggesting a stable attachment of protein on Erythrocyte$_{nex}$ and targeted release in the lung capillaries. We analyzed lung sections to investigate the distribution of OVA/Erythrocyte$_{nex}$ within the microstructures of lung. As shown in Figure 3g, the engineered OVA/Erythrocyte$_{nex}$ system was able to deliver a substantial amount of cargo and was highly distributed in these "hard-to-reach" capillary vascular microstructures. These results of lung-targeting property and permitted excretion of OVA/Erythrocyte$_{nex}$ were also supported by the biodistribution data of erythrocytes stained with CellTrace Far Red (Figure S12, Supporting Information). For up to 12 h after intravenous administration, erythrocyte engineered with Cellnex exhibited enhanced accumulation in the lung as compared to the naïve erythrocytes. However, after 24 h, erythrocytes engineered with Cellnex were found to have a similar biodistribution as the naïve erythrocytes.

The unique "particle-free" targeting performance of the Erythrocyte$_{nex}$ was further investigated in the biomimetic perfusion chamber experiments (Figure 3h and Figure S13, Supporting Information). In the microfluidic experiments, erythrocytes and OVA/Erythrocyte$_{nex}$ were flown at 10% hematocrit through 100 by 100 μm microfluidic channels coated with a confluent monolayer of endothelial cells mimicking the blood vessel wall (Figures S14–S16, Supporting Information). To verify the integrity of adhered Erythrocyte$_{nex}$, we compared the near-wall concentration distribution of cells in brightfield images. We observed a significant reduction of the cell-free layer thickness in the case of Erythrocyte$_{nex}$ when compared to naïve erythrocytes (Figure 3h,i). Moreover, fluorescence microscopy images confirmed the adhesion of Erythrocyte$_{nex}$ to the channel wall under physiological flow conditions (Figure 3i). The formation of a micron-sized cell-free layer near blood vessel walls under flow, commonly known as the Fåhræus–Lindqvist effect, can be explained by the balance between a lift force acting away from the wall due to erythrocyte deformability and shear-induced diffusion due to the hydrodynamic interactions among erythrocytes (Figure 3j and Section 14, Figure S17, Supporting Information). Using an existing theory,[43,44] we estimated the cross-flow concentration distributions of erythrocytes and Erythrocyte$_{nex}$ and the resulting cell-free layer thickness with (Figure 3j, red plot) or without wall adhesion (Figure 3j, green plot). We theoretically predicated that at matching flow conditions and cell mechanical properties, the cell-free layer thickness reduces from 17 μm for naïve erythrocytes to 0 for Erythrocyte$_{nex}$ due to wall adhesion, consistent with our experimental observations. Assuming a reversible adhesion process at intermediate rates, the theory estimated that 7% of Erythrocyte$_{nex}$ will remain adhered at steady state with a 6% increase in residence time, reducing the hematocrit in the flowing blood stream (Figure 3j, red plot). The adhesive property of Erythrocyte$_{nex}$ onto vessel walls is not specific to the endothelial cells (Figures S18 and S19, Supporting Information). Despite it being a reversible and transient process, this adhesion slows down Erythrocyte$_{nex}$ from the fast-flowing blood environment and can contribute to the overall prolonged retention time and lung targeting for drug delivery.

We also studied the adaptability of the Cellnex platform to engineer other mammalian cells apart from erythrocytes. Cell-based therapies (e.g., adoptive cell transfer and stem cell treatments) have been regarded as a promising approach to treat cancer and, more increasingly, autoimmune diseases. Tunable engineering of cells intended for transplantation is vital to maximize the efficacy of the administered cell therapies.[45] Common approaches for modulating immunosuppressive microenvironments, particularly within tumor sites, include targeting checkpoint pathways, modulating metabolic pathways, and generating cytokine-producing T cells.[46,47] These cellular modulation goals may be addressed by the present study of Cellnex. In the case of using cells as delivery vehicles (e.g., monocytes, macrophages), one approach to accelerate the time needed for cell preparation is to efficiently load biomolecule payloads onto cells without affecting their intrinsic ability to home to specific tissues.[48] For example, targeting monocyte differentiation pathways for specific macrophage phenotypes without adversely affecting their trafficking is necessary to achieve successful delivery. In the case of using transplanted cells (e.g., NK cells, T cells, and stem cells) as therapeutic entities, fine control over their activation and behavior allows for a personalized immunotherapeutic approach.[10] Prominent strategies include adoptive cell transfer with tumor-infiltrating lymphocytes, CAR T cells, and T cell receptor gene therapy, all of which modify the immune system to recognize tumor cells and carry out an anti-tumor effector function. Transplanted T and NK cell therapies usually require engineering with an adjuvant biomolecule (e.g., IL-12, IL-15) to keep the cells active. **Figure 4**a shows that the generalized Cellnex toolbox can be applied to a variety of mammalian cells. We used Alexa 488-conjugated BSA as a model biomolecule for integration with a range of cell types, including monocytes, macrophages, NK cells, T cells, dendritic cells, and cancer cells. Figure 4b illustrates the uniform and thin fluorescent layer on the surfaces of all types of cells, indicating the successful assembly of biomolecules on these cells and creation of at least six different types of Cellnex biohybrid systems with potentials of different biological functions.

To investigate the influence of the polyphenol-functionalized nanocomplexes on the cellular functions, we selected macrophages as a model to prepare a macrophage-based Cellnex system named as Macrophage$_{nex}$. We first studied the effect of nanocomplexes on the cellular properties of macrophages. The adaptation of Cellnex to different types of cellular systems and payload biomolecules requires the tuning of the nanocomplexes and Fe^{3+} used for the metal–phenolic coordination-mediated assembly. Thus, we studied the cell viability of Macrophage$_{nex}$ in the presence of different concentrations of nanocomplexes and Fe^{3+} ions. Figure S20 (Supporting Information) shows that only minor changes of cell viability can be seen when the concentrations of nanocomplexes and Fe^{3+} are lower than 96 μg mL^{-1} (nanocomplexes) and 180 μg mL^{-1} (Fe^{3+}), respectively. Figures S21 and S22 (Supporting Information) show that the integration of biological active species through the polyphenol-functionalized nanocomplexes showed neglected effect on the cell proliferative capability and chemotaxis capability toward an MCP-1 chemokine gradient. Moreover, macrophages maintained their phagocytotic capability after the integration of polyphenol-functionalized nanocomplexes (Figure S23, Supporting Information). Confocal fluorescence microscopy imaging validated that the nanocomplexes remained on cell

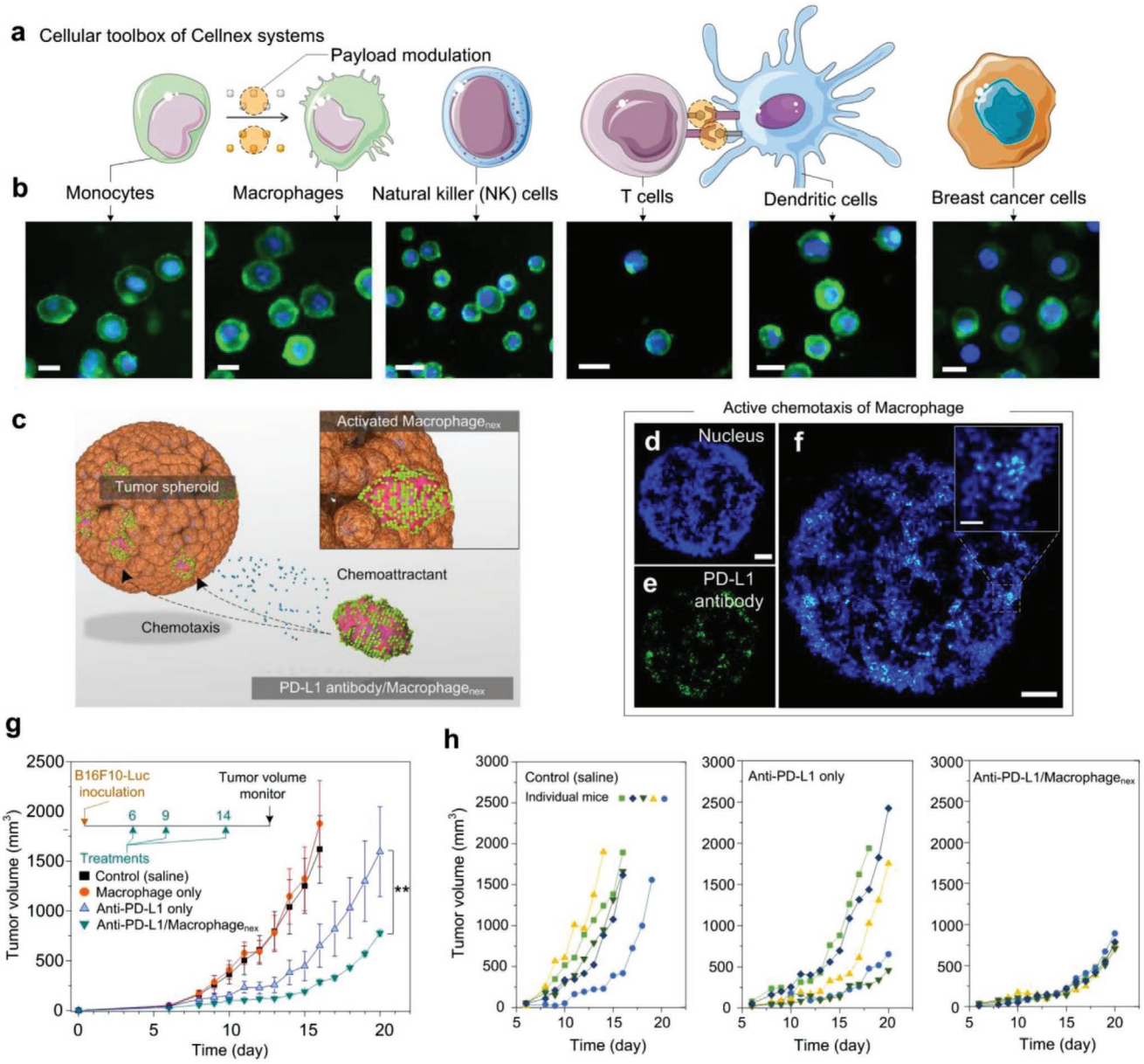

Figure 4. Versatile cellular toolbox of Cellnex and the engineered Macrophage$_{nex}$ for sensing and chemotaxis. a) Schematic diagram of the biological functions and crosstalk between the cellular components of the immune system. b) Cellnex allows the engineering of cell-based biohybrid systems from six types of cells. Alexa-Fluor-488-conjugated BSA was used to visualize the assembly of protein nanocomplexes on the cell surface. c) Schematic illustration of sensing and activation of Macrophage$_{nex}$. Alexa-Fluor-488-conjugated anti-PD-L1 antibody was used as a model of biologically active molecules. Confocal fluorescence microscopy image of a representative 4T1 breast cancer tumor spheroid. d) Blue represents 40,6-diamidino-2-phenylindole (DAPI), a nuclear stain. e) Green represents Macrophage$_{nex}$ carrying Alexa-Fluor-488-conjugated anti-PD-L1 antibody. f) The overlapped images of (d) and (e). The signal of anti-PD-L1 antibody was observed throughout the 4T1 breast cancer tumor spheroid. Scale bars are 10 µm (b), 50 µm ((d) and (e)), 100 µm, and 20 µm ((f) and inset). g) Overall tumor growth curve monitored at different time-points (n = 5). Inset shows the treatment schedule. Significantly different (two-way ANOVA followed by Tukey's HSD test): $^{**}p < 0.01$. Variation is represented by SE (error bars) for all data points. h) Tumor growth curve of individual mice in different treatment groups. The PD-L1 only group showed a low response rate (≈40%); however, the anti-PD-L1/Macrophage$_{nex}$ group exhibited a significant increase of the response rate (≈100%).

surfaces without internalization by cells (Figure S24, Supporting Information). Then, an immune checkpoint inhibitor (i.e., PD-L1 antibody) was used to integrate with Macrophage$_{nex}$ (Figure 4c), and its chemotaxis capability toward tumor spheroids was studied. Microscopy images show the compact cellular structure of the 4T1 tumor spheroid, which generally leads to the challenge of drug delivery into the central area and formation of drug resistance (Figure 4d and Figure S25, Supporting Information). Interestingly, anti-PD-L1/Macrophage$_{nex}$ was able to deliver the PD-L1 antibody to the tumor spheroid, even deeply into its center (Figure 4e,f). There was minimal penetration of fluorescence signal when free PD-L1 antibodies

were added into the tumor spheroid culture media (Figure S26, Supporting Information).

We then examined the potential of anti-PD-L1/Macrophage$_{nex}$ to improve the efficacy of immune checkpoint blockade therapy in vivo. A melanoma xenograft model was established by injecting B16F10-Luc cells into the mammary fat pad of immune-competent mice, wherein we designed a series of control experiments in which the presence of anti-PD-L1, isotype control IgG, and macrophage was varied. The tumor progression was significantly slowed after treatment with the anti-PD-L1 only and anti-PD-L1/Macrophage$_{nex}$ when compared to the control groups of macrophage only and saline (Figure 4g,h and Figure S27, Supporting Information). Particularly, on day 16, the untreated group showed a large tumor volume of 1619 ± 339 mm^3. The treatment by macrophage alone did not suppress the tumor growth. In a sharp contrast, the average tumor size of the group treated by anti-PD-L1/Macrophage$_{nex}$ was 285 ± 26 mm^3, which indicates a better therapeutic efficacy over the free anti-PD-L1 group (653 ± 217 mm^3), likely due to the enhanced delivery of the antibody to tumor as indicated by the tumor spheroid data shown in Figure 4c–f. In a separate study, a control group of Macrophage$_{nex}$ integrated with an innocuous protein isotype IgG (IgG/Macrophage$_{nex}$) revealed no improved inhibition of tumor growth compared with saline control group, indicating that the therapeutic outcomes of the anti-PD-L1/Macrophage$_{nex}$ was likely due to the targeted delivery of anti-PD-L1 to the tumor sites (Figure S28, Supporting Information). Meanwhile, the body weights of the mice were monitored over the course of the treatment period (Figure S29, Supporting Information). The body weight of the anti-PD-L1/Macrophage$_{nex}$ group showed no notable change.

In summary, the modular engineering of Cellnex offers a simple and adaptable method in which the biomolecules are simply mixed with polyphenols in an optimized stoichiometric ratio to form a nanoscale complexation, followed by subsequent assembly on the surfaces of various living cells. The Cellnex can be rapidly prepared (in less than 10 min), although it cannot eliminate the cell expansion process in cases that cell expansion is absolutely needed. We demonstrated that Cellnex enables a customizable cell-engineering platform with flexible toolboxes of carried biomolecules and cells. The Erythrocyte$_{nex}$ exhibited the ability to selectively target capillary vascular structures, which could be useful for the effective delivery of therapeutic drugs to lung cancer or chronic respiratory infections. As another example, Macrophage$_{nex}$ integrated with PD-L1 antibodies were able to penetrate into 4T1 breast cancer tumor spheroids through chemotaxis. An enhanced therapeutic efficiency of anti-PD-L1/Macrophage$_{nex}$ was also observed in the following in vivo experiments. With continuous development in the creation of new functional molecules and therapies, this simple and generalizable approach presents a promising platform for a wide range of cell-based therapies and biohybrid cell engineering.

Supporting Information

Supporting Information is available from the Wiley Online Library or from the author.

Acknowledgements

This work was financially supported by the Wyss Institute for Biologically Inspired Engineering at Harvard University (S.M.). N.K. was supported by the National Science Foundation Graduate Research Fellowship under Grant No. 1122374. All experiments were performed according to the approved protocols by the Institutional Animal Care and Use Committee (IACUC) of the Faculty of Arts and Sciences (FAS), Harvard University, Cambridge.

Conflict of Interest

S.M. and J.G. are inventors on a patent application (owned and managed by Harvard University) that covers some aspects of the technology described in the manuscript.

Author contributions

Z.Z. and D.P. contributed equally to this work. J.G., Z.Z., and S.M. conceived the ideas. Z.Z. and D.C.P. conducted the cell and in vivo experiments. Q.M.Q. conceived the modeling approach and performed the microfludic simulations and the corresponding data analysis. J.K. and C.J.K. performed the cargo release measurements. J.K., L. L.-W. W., T.S., N.K., C.W.S., D.W., and W.H. assisted with the cell experiments and contributed to the general methodology. Z.Z., D.C.P., Q.M.Q., J.G., and S.M. drafted the manuscript. All authors discussed the results and commented on the manuscript.

Keywords

biomolecules, cell therapy, erythrocytes, macrophages, polyphenol

Received: May 21, 2020
Revised: September 15, 2020
Published online: November 4, 2020

[1] R. A. Barker, J. Drouin-Ouellet, M. Parmar, *Nat. Rev. Neurol.* **2015**, *11*, 492.
[2] T. R. Heathman, A. W. Nienow, M. J. McCall, K. Coopman, B. Kara, C. J. Hewitt, *Regener. Med.* **2015**, *10*, 49.
[3] T. Li, H. Dong, C. Zhang, R. Mo, *Nano Res.* **2018**, *11*, 5240.
[4] X. Gong, J. Li, T. Tan, Z. Wang, H. Wang, Y. Wang, X. Xu, Z. Zhang, Y. Li, *Adv. Funct. Mater.* **2019**, *29*, 1903441.
[5] Y. Shi, T. Lammers, *Acc. Chem. Res.* **2019**, *52*, 1543.
[6] S. A. Rosenberg, N. P. Restifo, *Science* **2015**, *348*, 62.
[7] S. Gill, C. H. June, *Immunol. Rev.* **2015**, *263*, 68.
[8] L. A. Johnson, J. Scholler, T. Ohkuri, A. Kosaka, P. R. Patel, S. E. McGettigan, A. K. Nace, T. Dentchev, P. Thekkat, A. Loew, *Sci. Transl. Med.* **2015**, *7*, 275ra22.
[9] Z. Chen, Z. Wang, Z. Gu, *Acc. Chem. Res.* **2019**, *52*, 1531.
[10] C. W. ShieldsIV, L. L.-W. Wang, M. A. Evans, S. Mitragotri, *Adv. Mater.* **2019**, *32*, 1901633.
[11] L. Schultz, C. Mackall, *Sci. Transl. Med.* **2019**, *11*, 2127.
[12] L. Zhang, R. A. Morgan, J. D. Beane, Z. Zheng, M. E. Dudley, S. H. Kassim, A. V. Nahvi, L. T. Ngo, R. M. Sherry, G. Q. Phan, *Clin. Cancer Res.* **2015**, *21*, 2278.
[13] M. S. Goldberg, *Nat. Rev. Cancer* **2019**, *19*, 587.
[14] J.-W. Yoo, D. J. Irvine, D. E. Discher, S. Mitragotri, *Nat. Rev. Drug Discovery* **2011**, *10*, 521.
[15] A. C. Anselmo, V. Gupta, B. J. Zern, D. Pan, M. Zakrewsky, V. Muzykantov, S. Mitragotri, *ACS Nano* **2013**, *7*, 11129.

[16] L. Tang, Y. Zheng, M. B. Melo, L. Mabardi, A. P. Castaño, Y.-Q. Xie, N. Li, S. B. Kudchodkar, H. C. Wong, E. K. Jeng, *Nat. Biotechnol.* **2018**, *36*, 707.
[17] R. Polak, R. M. Lim, M. M. Beppu, R. N. Pitombo, R. E. Cohen, M. F. Rubner, *Adv. Healthcare Mater.* **2015**, *4*, 2832.
[18] M. T. Stephan, J. J. Moon, S. H. Um, A. Bershteyn, D. J. Irvine, *Nat. Med.* **2010**, *16*, 1035.
[19] C. W. Shields, M. A. Evans, L. L.-W. Wang, N. Baugh, S. Iyer, D. Wu, Z. Zhao, A. Pusuluri, A. Ukidve, D. C. Pan, *Sci. Adv.* **2020**, *6*, 6579.
[20] N. L. Klyachko, R. Polak, M. J. Haney, Y. Zhao, R. J. G. Neto, M. C. Hill, A. V. Kabanov, R. E. Cohen, M. F. Rubner, E. V. Batrakova, *Biomaterials* **2017**, *140*, 79.
[21] Y. Zhang, N. Li, H. Suh, D. J. Irvine, *Nat. Commun.* **2018**, *9*, 6.
[22] J. S. Brenner, D. C. Pan, J. W. Myerson, O. A. Marcos-Contreras, C. H. Villa, P. Patel, H. Hekierski, S. Chatterjee, J.-Q. Tao, H. Parhiz, *Nat. Commun.* **2018**, *9*, 2684.
[23] I. Zelepukin, A. Yaremenko, V. Shipunova, A. Babenyshev, I. Balalaeva, P. Nikitin, S. Deyev, M. Nikitin, *Nanoscale* **2019**, *11*, 1636.
[24] W. Zhu, J. Guo, Y. Ju, R. E. Serda, J. G. Croissant, J. Shang, E. Coker, J. O. Agola, Q. Z. Zhong, Y. Ping, *Adv. Mater.* **2019**, *31*, 1806774.
[25] J. J. Richardson, J. Cui, M. Björnmalm, J. A. Braunger, H. Ejima, F. Caruso, *Chem. Rev.* **2016**, *116*, 14828.
[26] J. Niu, D. J. Lunn, A. Pusuluri, J. I. Yoo, M. A. O'Malley, S. Mitragotri, H. T. Soh, C. J. Hawker, *Nat. Chem.* **2017**, *9*, 537.
[27] J. H. Park, K. Kim, J. Lee, J. Y. Choi, D. Hong, S. H. Yang, F. Caruso, Y. Lee, I. S. Choi, *Angew. Chem.* **2014**, *126*, 12628.
[28] B. J. Kim, H. Cho, J. H. Park, J. F. Mano, I. S. Choi, *Adv. Mater.* **2018**, *30*, 1706063.
[29] J. Guo, B. L. Tardy, A. J. Christofferson, Y. Dai, J. J. Richardson, W. Zhu, M. Hu, Y. Ju, J. Cui, R. R. Dagastine, *Nat. Nanotechnol.* **2016**, *11*, 1105.
[30] J. Guo, M. Suástegui, K. K. Sakimoto, V. M. Moody, G. Xiao, D. G. Nocera, N. S. Joshi, *Science* **2018**, *362*, 813.
[31] H. A. Lee, Y. Ma, F. Zhou, S. Hong, H. Lee, *Acc. Chem. Res.* **2019**, *52*, 704.
[32] M. Shin, H.-A. Lee, M. Lee, Y. Shin, J.-J. Song, S.-W. Kang, D.-H. Nam, E. J. Jeon, M. Cho, M. Do, *Nat. Biomed. Eng.* **2018**, *2*, 304.
[33] C. H. Villa, A. C. Anselmo, S. Mitragotri, V. Muzykantov, *Adv. Drug Delivery Rev.* **2016**, *106*, 88.
[34] Y. Qiu, D. R. Myers, W. A. Lam, *Nat. Rev. Mater.* **2019**, *4*, 294.
[35] J. Shi, L. Kundrat, N. Pishesha, A. Bilate, C. Theile, T. Maruyama, S. K. Dougan, H. L. Ploegh, H. F. Lodish, *Proc. Natl. Acad. Sci. USA* **2014**, *111*, 10131.
[36] S. Mitragotri, P. A. Burke, R. Langer, *Nat. Rev. Drug Discovery* **2014**, *13*, 655.
[37] N. Pishesha, A. M. Bilate, M. C. Wibowo, N.-J. Huang, Z. Li, R. Deshycka, D. Bousbaine, H. Li, H. C. Patterson, S. K. Dougan, *Proc. Natl. Acad. Sci. U. S. A.* **2017**, *114*, 3157.
[38] Y. Alapan, O. Yasa, O. Schauer, J. Giltinan, A. F. Tabak, V. Sourjik, M. Sitti, *Sci. Robot.* **2018**, *3*, 4423.
[39] J. Guo, T. Suma, J. J. Richardson, H. Ejima, *ACS Biomater. Sci. Eng.* **2019**, *5*, 5578.
[40] C. Zhang, B. Wu, Y. Zhou, F. Zhou, W. Liu, Z. Wang, *Chem. Soc. Rev.* **2020**, *49*, 3605.
[41] W. M. Usman, T. C. Pham, Y. Y. Kwok, L. T. Vu, V. Ma, B. Peng, Y. San Chan, L. Wei, S. M. Chin, A. Azad, *Nat. Commun.* **2018**, *9*, 2359.
[42] J. Guo, Y. Ping, H. Ejima, K. Alt, M. Meissner, J. J. Richardson, Y. Yan, K. Peter, D. Von Elverfeldt, C. E. Hagemeyer, *Angew. Chem., Int. Ed.* **2014**, *53*, 5546.
[43] Q. M. Qi, E. Dunne, I. Oglesby, I. Schoen, A. J. Ricco, D. Kenny, E. S. Shaqfeh, *Biophys. J.* **2019**, *116*, 1136.
[44] R. G. H. Rivera, X. Zhang, M. D. Graham, *Phys. Rev. Fluids* **2016**, *1*, 060501.
[45] M. O. Dellacherie, B. R. Seo, D. J. Mooney, *Nat. Rev. Mater.* **2019**, *4*, 379.
[46] S. Mardiana, B. J. Solomon, P. K. Darcy, P. A. Beavis, *Sci. Transl. Med.* **2019**, *11*, 2293.
[47] Q. Sun, M. Barz, B. G. De Geest, M. Diken, W. E. Hennink, F. Kiessling, T. Lammers, Y. Shi, *Chem. Soc. Rev.* **2019**, *48*, 351.
[48] A. C. Anselmo, J. B. Gilbert, S. Kumar, V. Gupta, R. E. Cohen, M. F. Rubner, S. Mitragotri, *J. Controlled Release* **2015**, *199*, 29.